Supplementary information: The role of topological defects in the two-stage melting and elastic behaviour of active Brownian particles

Siddharth Paliwal* and Marjolein Dijkstra†
Soft Condensed Matter, Debye Institute for Nanomaterials Science, Utrecht University, Princetonplein 1, 3584 CC Utrecht, The Netherlands
(Dated: October 11, 2019)

I. MODEL

We consider a two-dimensional system of isotropic Brownian particles that exhibit a self-propulsion speed v_0 which is directed along the orientation vector $\mathbf{e}_i = (\cos\theta_i, \sin\theta_i)$ assigned to particle $i \in 1, \ldots, N$. To describe the translational and rotational motion of the individual colloidal particle we employ the overdamped Langevin dynamics:

$$\begin{aligned} \gamma\dot{\mathbf{r}}_i &= -\sum_{j\neq i} \boldsymbol{\nabla}_i \mathrm{U}(\mathrm{r}_{ij}) + \gamma v_0 \mathbf{e}_i + \sqrt{2\gamma k_B T}\boldsymbol{\Lambda}_i^t, \\ \dot{\theta}_i &= \sqrt{2D_r}\Lambda_i^r, \end{aligned} \tag{S1}$$

where γ is the damping coefficient due to the drag forces from the implicit solvent, k_B is the Boltzmann constant, and T is the bath temperature. D_r is the rotational diffusion coefficient. The quantities $\boldsymbol{\Lambda}_i^t$ and Λ_i^r are unit-variance Gaussian noise terms with zero mean:

$$\begin{aligned} \left\langle \boldsymbol{\Lambda}_i^t(t) \right\rangle &= 0, \qquad \left\langle \Lambda_i^r(t) \right\rangle = 0, \\ \left\langle \boldsymbol{\Lambda}_i^t(t)\boldsymbol{\Lambda}_j^t(t') \right\rangle &= \mathbb{I}_2 \delta_{ij}\delta(t-t') \\ \left\langle \Lambda_i^r(t)\Lambda_j^r(t') \right\rangle &= \delta_{ij}\delta(t-t'), \end{aligned} \tag{S2}$$

where $\mathbb{I}_2$ is the 2×2 identity matrix. The angular brackets $\langle \cdots \rangle$ denote an average over different realizations of the noise. The particles interact with a short-range repulsive Weeks-Chandler-Andersen (WCA) potential given by:

$$\begin{aligned} \mathrm{U}(\mathrm{r}) &= 4\varepsilon\left[\left(\frac{\sigma}{\mathrm{r}}\right)^{12} - \left(\frac{\sigma}{\mathrm{r}}\right)^{6}\right] + \varepsilon, && \mathrm{r} \leq 2^{1/6}\sigma \\ &= 0 && \mathrm{r} > 2^{1/6}\sigma \end{aligned} \tag{S3}$$

where $\mathrm{r} = |\mathbf{r}_{ij}|$ is the distance between the centers of particle i and j, σ is the particle diameter pertaining to the length scale in WCA potential, and ε is the strength of the particle interactions.

We set the system temperature $k_BT/\varepsilon = 1$, following Ref. [1], and the damping coefficient $\gamma\sigma^2/\varepsilon = 1$ fixing the translational diffusion coefficient to correspond to the free diffusion of particles given by the Stokes-Einstein relation $D_t = \gamma^{-1}k_BT$. This sets our time scale as $\tau = \gamma\sigma^2/k_BT$. The rotational diffusion coefficient is set to $D_r\tau = 3$ and we use a time step size $dt = 10^{-5}\tau$ for numerically integrating the equations of motion. We define a non-dimensional Péclet number $\mathrm{Pe} = v_0\tau/\sigma$ as the ratio of the persistence length of motion to the particle diameter and perform simulations using the HOOMD-Blue [2, 3] package in the range $0 \leq \mathrm{Pe} \leq 150$. We used $N = 72\times10^3$ particles in an approximately square 2D periodic simulation box with dimensions $L_x, L_y \approx 250\sigma$ for identifying the fluid-hexatic-solid transitions and $N = 2.8\times10^3$ for calculating the elastic moduli. We used a regular hexagonally packed arrangement of particles at the overall system density as our initial configuration and we collect snapshots for $200\tau - 500\tau$ at an interval of τ for analysis after allowing the system to achieve a stationary state for about 200τ.

As mentioned in the main text, the state diagram shown in Fig. 1 was obtained by measuring the equation of state (pressure-density curves), the density histograms, the decay of the orientational and positional correlation functions to locate the boundaries as precisely as possible. Specifically, to locate the coexistence, we identified negative slope regions in the pressure-density curves as well as double-peaked structure of the density histograms similar to the analysis presented in Ref. [4] and Ref. [5]. We describe below the orientational and positional order parameters used for identifying the hexatic and solid phases.

* s.paliwal@uu.nl
† m.dijkstra@uu.nl

II. ORIENTATIONAL AND POSITIONAL ORDER

We measure the local 6-fold orientational symmetry around particle i using the hexatic order parameter $\psi_6(\mathbf{r}_i)$ given by:

$$\psi_6(\mathbf{r}_i) = \frac{1}{N_b} \sum_{j \in N_b} \exp(\iota 6\theta_{ij}), \tag{S4}$$

where N_b denotes the number of nearest neighbors of particle i, identified using a Voronoi construction, and the bond angle θ_{ij} is measured as a deviation of the orientation of the vector $\mathbf{r}_{ij}$ from the reference global system orientation measured from $\Psi_6(L)$ averaged over all the particles. We study the decay of the spatial orientational correlation function $g_6(\mathrm{r})$ expressed as:

$$g_6(\mathrm{r}) = \langle \psi_6^*(\mathbf{r}' + \mathbf{r}) \psi_6(\mathbf{r}') \rangle. \tag{S5}$$

From the KTHNY theory, the equilibrium hexatic phase exhibits quasi long-range orientational order which decays algebraically as $g_6(\mathrm{r}) \propto r^{-\eta_6}$ with an exponent $0 \leq \eta_6 \leq 1/4$, and the liquid phase is characterized by an exponential decay of $g_6(\mathrm{r})$. We use the same criteria to identify the liquid-hexatic phase transition boundary in Fig.1 in the main text.

To investigate the decay of positional order, we measure the positional correlation function

$$g_T(\mathrm{r}) = \langle \psi_T^*(\mathbf{r}' + \mathbf{r}) \psi_T(\mathbf{r}') \rangle, \tag{S6}$$

where $\psi_T(\mathbf{r}_i)$ is the positional order parameter expressed as:

$$\psi_T(\mathbf{r}_i) = \exp(\iota \mathbf{k}_0 \cdot \mathbf{r}_i). \tag{S7}$$

Here $\mathbf{k}_0$ is the vector in reciprocal space denoting one of the first Bragg peaks in the 2D structure factor $S(\mathbf{k})$. The magnitude of this vector is equal to that of the reciprocal lattice vector i.e. $\mathbf{k}_0 = (0, 4\pi/a\sqrt{3})$ where $a = (2/\rho\sqrt{3})^{1/2}\sigma$ is the lattice spacing in a regular hexagonal packing at a number density ρ in a 2D geometry. According to the KTHNY theory, the positional order of a two-dimensional solid decays algebraically as $g_T(r) \propto r^{-\eta_T}$ with an exponent $0 \leq \eta_T \leq 1/3$. Upon melting, the decay of the positional correlations becomes exponential i.e. $g_T(r) \propto \exp(-r/\xi_T)$ with a correlation length ξ_T, which decreases with decreasing density. For each case, we measure the positional correlation functions $g_T(r)$ up to an interparticle separation of $r = L/2$ with L the box length. The measurements are averaged over multiple configurations, at an interval of 0.5-1 τ to yield the curves shown in Fig. S1 and Fig. S2. We show the $g_T(r)$ curves as a function of particle separation r in Fig. S1 and extract the correlation lengths ξ_T in the case of an exponential decay or the exponent η_T in the case of an algebraic decay.

In Fig. S1, for Pe = 0 we can clearly identify the change from an exponential to algebraic decay upon changing the density from 0.920 to 0.926. However, for Pe $\geq$ 7.2 the decay does not fit either an algebraic or an exponential decay for the full range of particle separations. For small r, the decay is close to an exponential with a large correlation length that may span the full simulation box for Pe $\geq$ 47.7. But for large r the decay is close to a polynomial decay. Hence, in order to identify the hexatic-solid transition in this case, we locate the density at which the exponent η_T of a polynomial fit to the tail of the correlation function becomes smaller than 1/3. For Pe = 0, we find that the decay of $g_T(r)$ becomes algebraic with $\eta_T \approx 1/3$ at $\rho\sigma^2 = 0.926$, marking the hexatic-solid phase transition. For Pe = 71.5 this transition is located near $\rho\sigma^2 = 1.900$.

In Fig. S3(a) and (b) we show typical particle configurations colored according to the angle of positional order parameter $\psi_T(\mathbf{r}_i)$. We can observe topological defects in the configurations for $\rho\sigma^2 = 1.420$ and 1.550 but not for $\rho\sigma^2 = 1.600$ and 1.950 with $N = 72 \times 10^3$ particles.

A. System-size dependence

To check the finite-size effects on the decay of the positional order we also simulate a few cases with larger system sizes up to $N = 2262 \times 10^3$ particles. We show the positional correlation function $g_T(r)$ for these different system sizes at Pe = 23.8 and 71.5 in Fig. S2. The values for the exponents η_T of the power-law decay fitted in the tail region marked by the dashed lines for each case, are also listed in the figure. For $N = 72 \times 10^3$ and both cases considered here, we observe clearly that $\eta_T < 1/3$, which corresponds to a solid phase. However, for $N \geq 288 \times 10^3$, we find that the exponent $\eta_T > 1/3$ increases with system size, indicating a faster decay for larger systems. Hence, all the systems with $N \geq 288 \times 10^3$ are identified as hexatic states, and the hexatic-solid transition shifts to higher densities for a larger number of particles N. Despite these differences in the decay of the positional correlations, the observed hexatic region devoid of any defects is robust for the investigated system sizes.

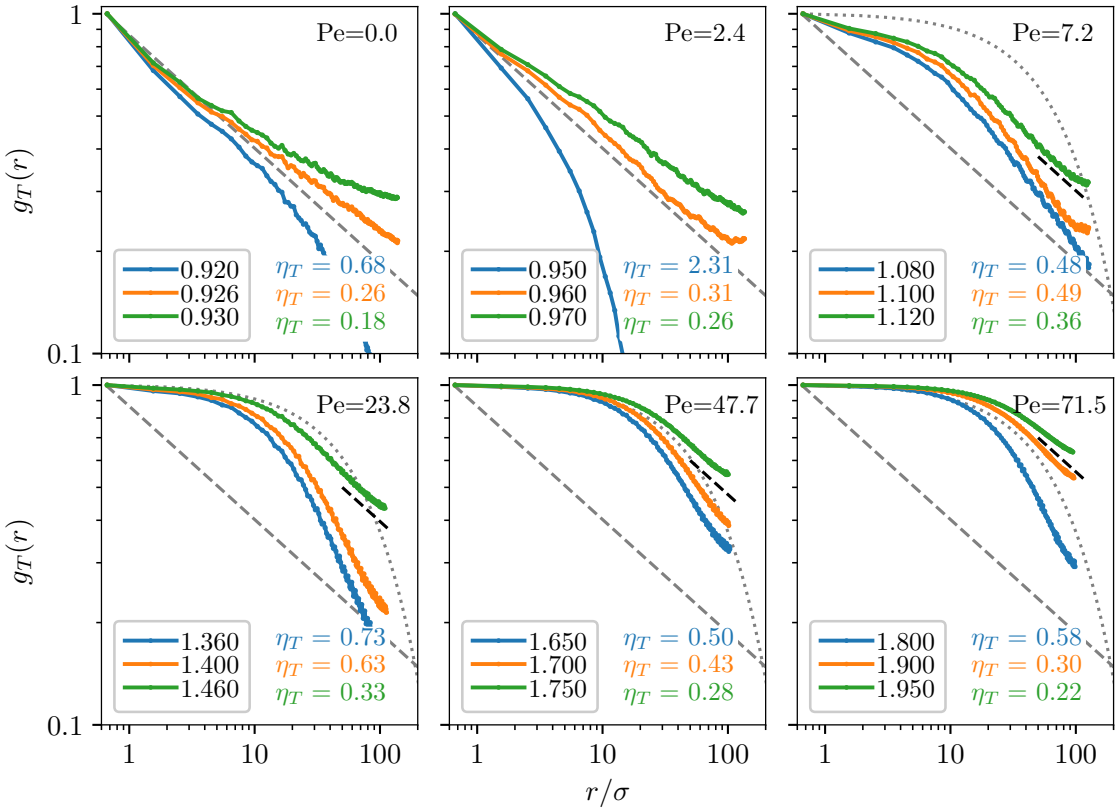

FIG. S1. Positional correlation function $g_T(r)$ for $0 \leq \mathrm{Pe} \leq 71.5$ at the labeled densities. The values for the exponents η_T, obtained by fitting the $g_T(r)$ with an algebraic decay, are also displayed in the figure. The decay is exponential for a hexatic state with a correlation length that increases with density, and the decay becomes quasi-long ranged for a crystalline state. The dashed grey lines indicate algebraic decay with an exponent $\eta_T = 1/3$ and the dotted grey lines indicate exponential decay with a correlation length 100σ.

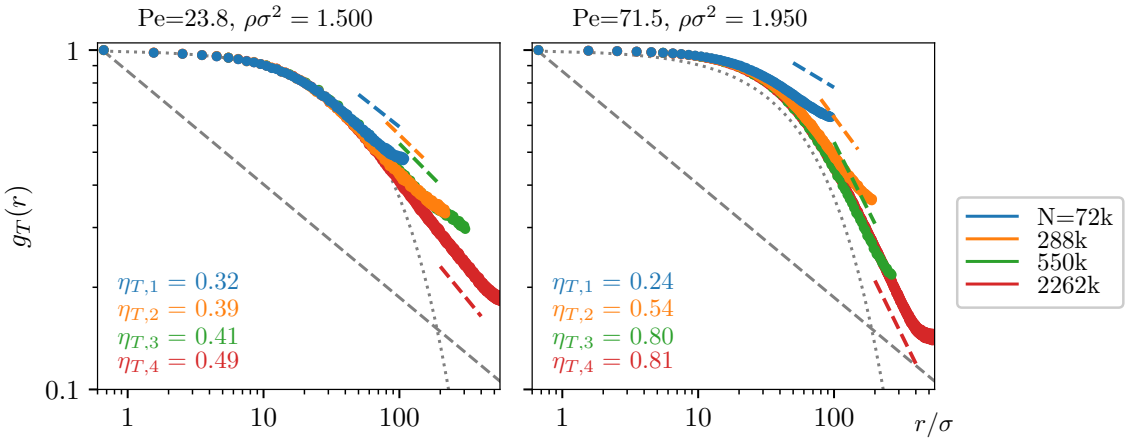

FIG. S2. Positional correlation function $g_T(r)$ for (left) Pe=23.8 and $\rho\sigma^2 = 1.500$, and (right) Pe=71.5 and $\rho\sigma^2 = 1.950$ for system sizes of $N = 72 \times 10^3$ (blue) identified as a crystalline state in Fig. S1, $N = 288 \times 10^3$ (orange), $N = 550 \times 10^3$ (green) and $N = 2262 \times 10^3$ (red). The values for the corresponding exponents η_T, obtained by fitting the $g_T(r)$ with an algebraic decay, are displayed in the figure, showing that these state points correspond to a hexatic state for $N \geq 288 \times 10^3$. The long-distance regime of the $g_T(r)$ is ignored in our fitting procedure. The grey dotted lines indicate an exponential decay with a correlation length $\xi_T = 100\sigma$, and the grey dashed lines indicate a power-law decay with exponent $\eta_T = 1/3$.

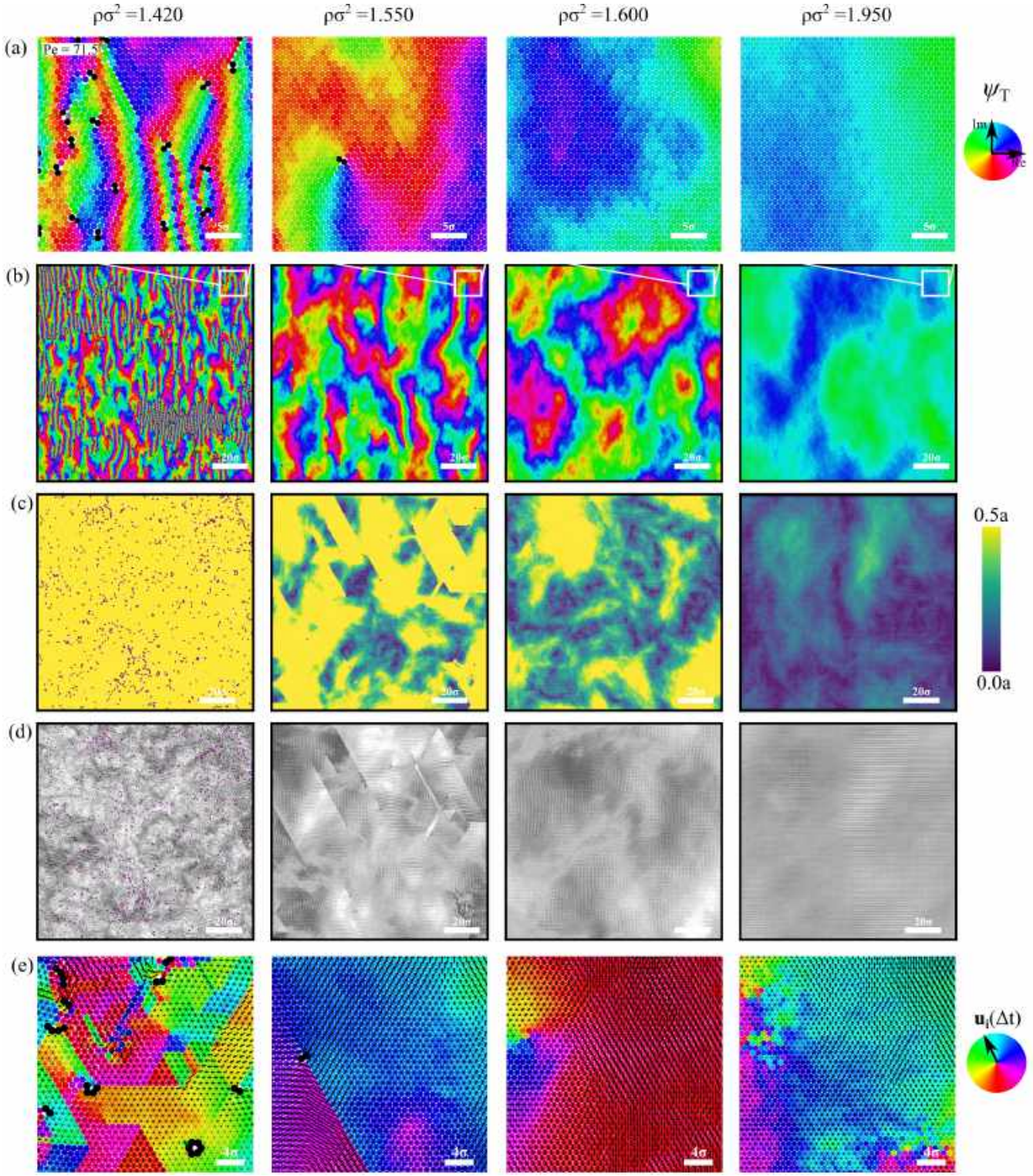

FIG. S3. Typical particle configurations in the high density region for Pe = 71.5 with the color scheme as follows: (a) and (b) as $\arg(\psi_T)$ after subtracting the mean orientation, as shown in the color wheel on the right where (a) is a magnification of (b), (c) magnitude of displacement vectors $|\mathbf{u}_i(\Delta t = 10\tau)|$ in units of lattice spacing a as shown in the legend, (d) displacement vectors $\mathbf{u}_i(\Delta t = 10\tau)$ as arrows with a normalizing scale factor, (e) magnified view of displacement vectors with background colors indicating the orientation of the $\mathbf{u}_i$ vector as shown in the color-wheel on the right. We observe topological defects in the configurations for $\rho\sigma^2 = 1.420$ and 1.550 but not for $\rho\sigma^2 = 1.600$ and 1.950 with $N = 72 \times 10^3$ particles.

III. COOPERATIVE MOTION

We note that the solid-hexatic transition at high Pe cannot be driven by changes in the concentrations of the topological defects as the defect-free solid melts into a hexatic phase devoid of any defects. Hence, we speculate that the solid-hexatic transition may be driven by a growing length scale of regions of cooperative motion. To corroborate this, we measure the particle displacement $\mathbf{u}_i(\Delta t) = \mathbf{r}_i(t + \Delta t) - \mathbf{r}_i(t)$ of particle $i \in 1, \cdots, N$ for Pe = 71.5 and for varying hexatic and solid states.

In Fig. S3, we show typical particle configurations of hexatic states at densities $\rho\sigma^2 = 1.420, 1.550$, and 1.600 and a solid state at density $\rho\sigma^2 = 1.950$ for Pe = 71.5 and $N = 72 \times 10^3$ particles. We display the defect particles in black in Fig. S3 (a), (b), and (e) and in blue (5-fold disclination) and red (7-fold disclination) in Fig. S3 (c) and (d). We observe topological defects in the configurations for $\rho\sigma^2 = 1.420$ and 1.550 but not for $\rho\sigma^2 = 1.600$ and 1.950, confirming that the hexatic-solid transition is not mediated by defects. In Fig. S3(a) and (b), the particles are colored according to $\arg(\psi_T)$ with ψ_T the local positional order parameter. Fig. S3(a) is a zoom-in of the area displayed by the white box in Fig. S3(b). We clearly observe that the range of the positional order increases with density. In Fig. S3(c), the particles are colored according to the magnitude of the displacement vectors $|\mathbf{u}_i|$. We clearly observe that the average magnitude of displacements decreases with increasing density and that the size of the regions with a similar $|\mathbf{u}_i|$, characterizing cooperative motion, increases. The growing length scale of regions of cooperative motion with increasing density can also be appreciated from the displacement maps in Fig. S3(d) and (e), which show the orientation of $\mathbf{u}_i$ as arrows and colors, respectively. The size of regions with a homogeneous color, denoting cooperative motion, increases with density and the system becomes more solid-like when the regions become system-spanning.

Displacement maps for $\mathbf{N = 2262 \times 10^3}$ particles

In addition, we also investigated the growing length scale of regions of cooperative motion for system sizes as large as $N = 2262 \times 10^3$ particles. We show the positional correlation functions $g_T(r)$ over a density range of $\rho\sigma^2 = 1.500$ to 2.150 in Fig. S4 from simulations with $N = 2262 \times 10^3$ particles for Pe=71.5. We collect particle configurations at a frequency of 0.5τ for a duration of 100τ after an equilibration run of about 50τ. We used a time step of $dt = 5 \times 10^{-6}\tau$ and each simulation required about 14400 CPU hours on a 1.4GHz AMD processor using a modified version of LAMMPS [6]. We fit the $g_T(r)$ with both an exponential decay as well as an algebraic decay, and present the correlation length ξ_T and exponent η_T in the figure. Even for the highest density that we were able to simulate within our computational resources, $\rho\sigma^2 = 2.150$, we did not observe a perfect algebraic decay with an exponent $\eta_T \leq 1/3$, and hence the system is identified as an hexatic state.

In Fig. S5, we show the displacement maps $\mathbf{u}_i(\Delta t = 1\tau)$ for system sizes as large as $N = 2262 \times 10^3$ particles using different representations. In Fig. S5(a), the particles are colored according to the direction of the displacements $\mathbf{u}_i(\Delta t = 1\tau)$. The size of regions with a homogeneous color, denoting cooperative motion, increases with density. In Fig. S5(b) and (c), we show the displacement vectors $\mathbf{u}_i$ as arrows. Fig. S5(c) is a zoom-in of the system. In addition, we color the defect particles as blue (5-fold disclination) and red (7-fold disclination) in Fig. S5(c). We clearly observe that the regions of cooperative motion increase in size upon increasing the density.

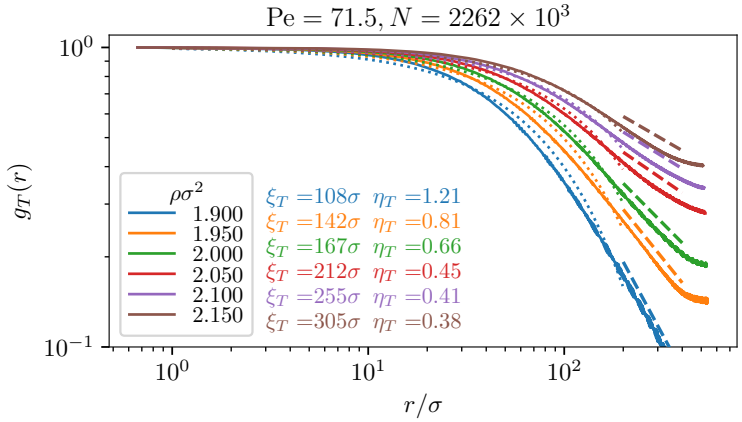

FIG. S4. Positional correlations $g_T(r)$ on a log − log scale for a system size of $N = 2262 \times 10^3$ for Pe= 71.5. The values for the correlation length ξ_T fitted in the region $(1\sigma - 200\sigma)$ and exponents η_T of the power-law decay fitted in the tail region are also quoted in the figure. The dotted lines indicate exponential fits and the dashed lines indicate power-law fits.

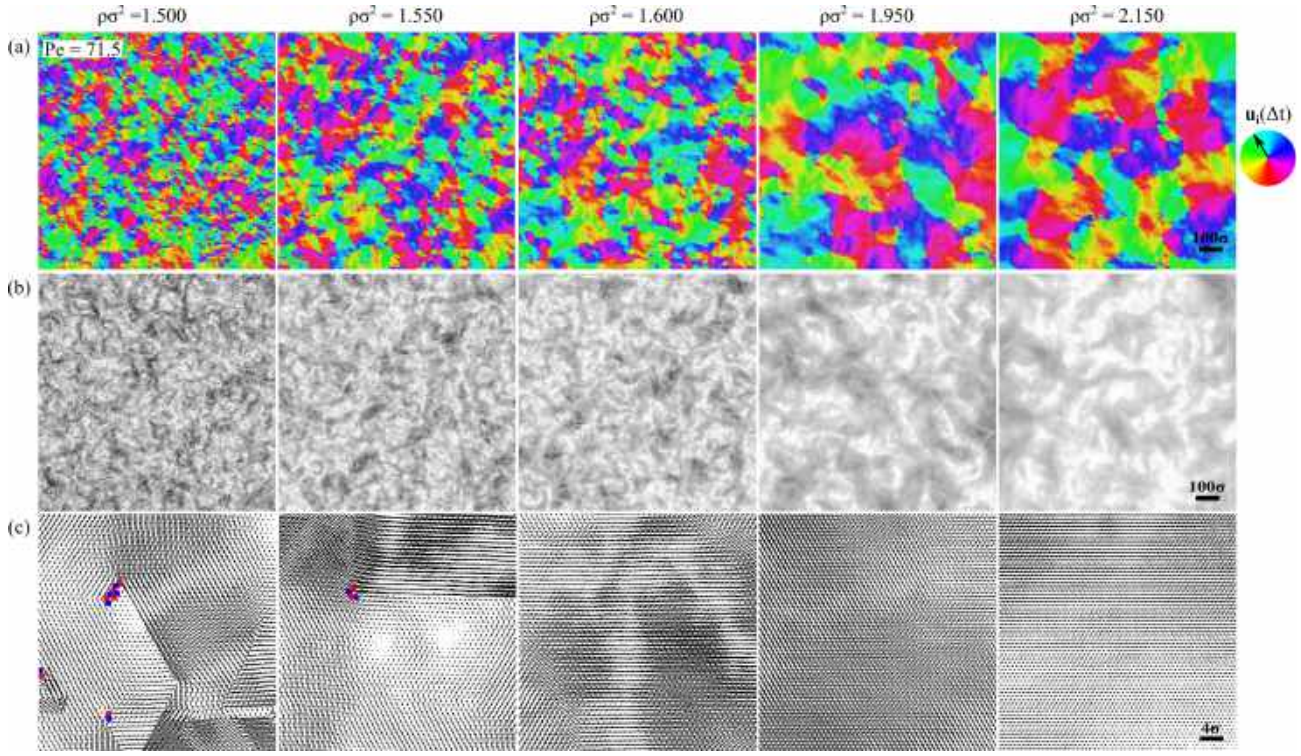

FIG. S5. Displacement maps for Pe = 71.5 and densities as labeled in the figure. In (a) the color indicates the orientation of the displacement vector $\mathbf{u}_i(\Delta t = 1\tau)$ as shown in the color-wheel on the right, showing an increase in the size of regions of cooperative movement with increasing density. In (b) and (c) we show the displacement vectors $\mathbf{u}_i(\Delta t = 1\tau)$ as arrows scaled by a normalizing factor. The bottom row is a magnification of the middle row.

Finally, we compare solid states for Pe = 0 and Pe = 71.5 for a system size of $N = 72 \times 10^3$ particles. We show the magnitude of the displacement vector $|\mathbf{u}_i(\Delta t = 10\tau)|$ in Fig. S6(a) and (b), and the vector $\mathbf{u}_i$ itself as arrows in Fig. S6(b) over a time interval of $\Delta t = 10\tau$. We color the defect particles as blue (5-fold disclination) and red (7-fold disclination). Fig. S6(b) is a zoom-in of the white box shown in Fig. S6(a). For the solid state at Pe = 0, the defect configurations are mainly bound dislocation pairs, and the dynamics appears to be heterogeneous. For a defect-free crystalline state at Pe = 71.5 and $\rho\sigma^2 = 1.950$, the dynamics is suppressed but more cooperatively. In addition, we add supplementary movies to show the displacement fields in time at Pe = 0 for a solid state, and at Pe = 71.5 for both a hexatic and a solid state.

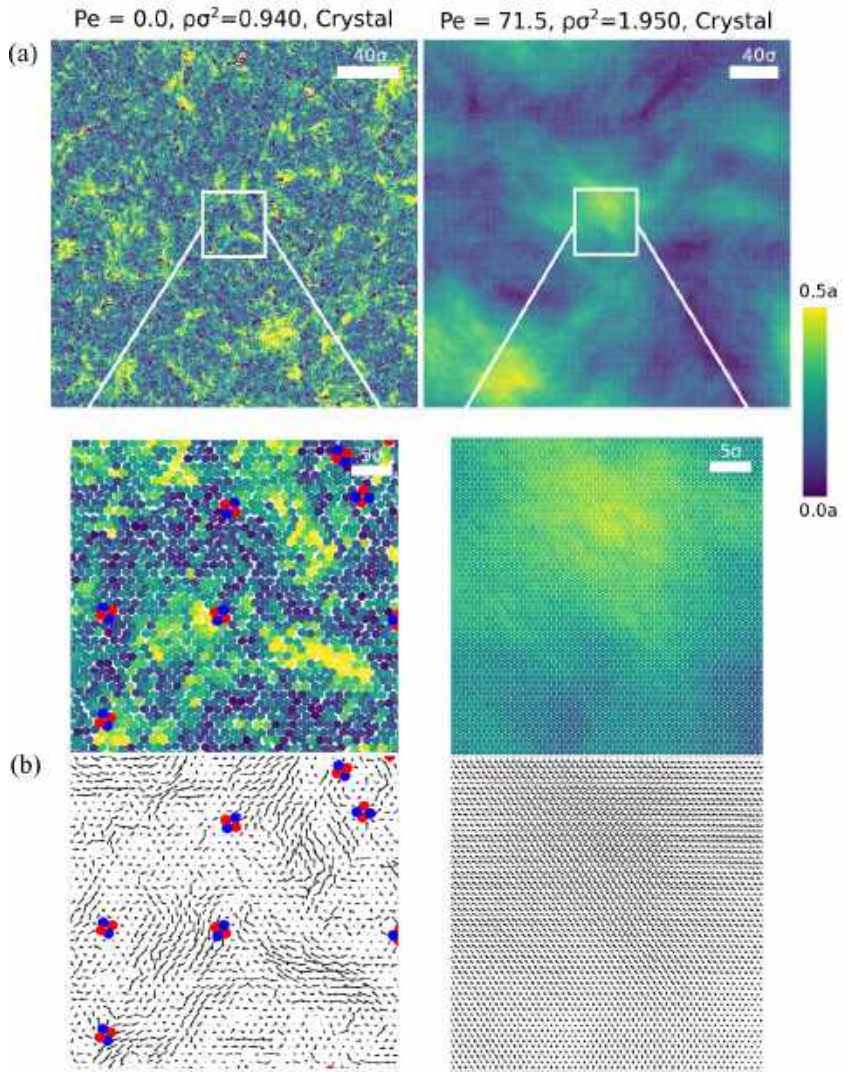

FIG. S6. (a) Magnitude of the displacement field $\mathbf{u}_i(\Delta t = 10\tau)$ for the states marked as crystalline in Fig.1 in the main text for Pe= 0.0 and 71.5. The color scale, in units of the lattice parameter $a = (2/\rho\sqrt{3})^{1/2}\sigma$, is shown on the right. (b) The displacement vectors $\mathbf{u}_i(\Delta t = 10\tau)$ as arrows with lengths scaled by a normalizing factor and the defects colored as per the convention defined in Fig.2 in the main text.

Movie 1a-1c show the displacement fields $\mathbf{u}_i(\Delta t = 10\tau)$ along with the defects (if present) for (1a) Pe=0.0 $\rho\sigma^2 = 0.940$ (solid state), (1b) Pe=71.5 $\rho\sigma^2 = 1.550$ (hexatic state) and (1c) Pe=71.5 $\rho\sigma^2 = 1.950$ (solid state).

Movie 2a-2b show the magnitude of positional order parameter ψ_T along with defects (if present) for (2a) Pe=0.0 $\rho\sigma^2 = 0.940$ (solid state) and (2b) Pe=71.5 $\rho\sigma^2 = 1.950$ (solid state).

IV. ELASTIC MODULI

A. Stress tensor

In order to measure the bulk pressure P in our system consisting of N active Brownian particles, we employ the expressions as introduced by Winkler *et al.*[7] for isotropic systems, but here we generalized these expressions to anisotropic systems in 2D. Specifically, the pressure for isotropic active particles in a periodic box with lateral dimensions L_x and L_y and 2D 'volume' $V = L_xL_y$ is calculated using $P = \mathrm{Tr}(\mathbb{P})$ where the full stress tensor $\mathbb{P}$ is given by:

$$P_{\alpha\beta} = P^{\mathrm{vir}}_{\alpha\beta} + \delta_{\alpha\beta}(P^{\mathrm{id}}_{\alpha\beta} + P^{\mathrm{swim}}_{\alpha\beta}). \tag{S8}$$

Here P^{id} is the ideal gas pressure given by $P^{\mathrm{id}} = \rho k_B T$ with $\rho = N/V$ the number density of the particles. The virial contribution P^{vir} is obtained using the standard virial expression

$$P^{\mathrm{vir}}_{\alpha\beta} = -\frac{1}{4V}\left\langle \sum_{i}^{N}\sum_{j\neq i}^{N} \boldsymbol{\partial}_{\mathbf{r}_{i,\beta}} \mathrm{U}(r_{ij}) \cdot (\mathbf{r}_{i,\beta} - \mathbf{r}_{j,\beta}) \right\rangle. \tag{S9}$$

The swim contribution $P^{\mathrm{swim}}_{\alpha\alpha}$ due to the self-propulsion is given by:

$$P^{\mathrm{swim}}_{\alpha\alpha} = \frac{\gamma\rho v_0^2}{2D_r} - \frac{\gamma v_0}{4VD_r}\left\langle \sum_{i=1}^{N}\sum_{j\neq i}^{N} \frac{\boldsymbol{r}_{ij,\alpha}\mathbf{e}_{i,\alpha}}{r_{ij}} \frac{\partial \mathrm{U}(r_{ij})}{\partial r_{ij}} \right\rangle. \tag{S10}$$

We note that the full stress tensor $P_{\alpha\beta}$ fully captures the anisotropy in finite -strain simulations. An alternative expression is also found in literature [8–10] which defines the swim stress tensor as the moment of swim force:

$$\mathbb{P}^{\mathrm{swim}} = \frac{\gamma v_0}{V}\left\langle \sum_{i=1}^{N} \mathbf{re} \right\rangle. \tag{S11}$$

This expression is identical to Eq. S10 as shown in Ref. [7] for isotropic systems. We verified that both expressions are identical by measuring explicitly the tensorial swim stress using both methods in finite -strain simulations.

B. Stiffness tensor and Lamé elastic coefficients

In the linear elastic theory of isotropic solids, the elastic moduli relate the stress response of a system to an applied strain. In equilibrium, the elastic moduli are related to the free energy change due to such deformations [11]. Instead, for non-equilibrium systems we directly assume Hooke's law which linearly relates the mechanical stress $P_{\alpha\beta}$ with the applied strain $\epsilon_{\gamma\delta}$ through a symmetric stiffness tensor $\mathbb{C}$ given by:

$$\mathbb{C} = \begin{bmatrix} C_{11} & C_{12} & 0 & 0 \\ & C_{22} & 0 & 0 \\ & & 0 & 0 \\ & & & C_{44} \end{bmatrix} = \begin{bmatrix} \lambda+2\mu & \lambda & 0 & 0 \\ & \lambda+2\mu & 0 & 0 \\ & & 0 & 0 \\ & & & \mu \end{bmatrix}$$

where λ and μ are the Lamé coefficients in equilibrium systems [11]. For conciseness, we follow the Voigt notation above for indexing $C_{\alpha\beta\gamma\delta}$ with xx=1, yy=2, and xy=4. If a system is under a uniform isotropic pressure, the stiffness tensor $\mathbb{C}$ can be rewritten in terms of an effective stiffness tensor $\mathbb{B}$ as [12, 13]:

$$B_{\alpha\beta\gamma\delta} = C_{\alpha\beta\gamma\delta} - P(\delta_{\alpha\gamma}\delta_{\beta\delta} + \delta_{\alpha\delta}\delta_{\beta\gamma} - \delta_{\alpha\beta}\delta_{\gamma\delta}) \tag{S12}$$

$$\begin{aligned} B_{11} &= C_{11} - P, \quad B_{22} = C_{22} - P, \\ B_{12} &= C_{12} + P, \quad B_{44} = C_{44} - P, \end{aligned}$$

where $P = (P_{xx} + P_{yy})/2$ is the uniform pressure. The bulk modulus E, the shear modulus G and the Young's modulus K are related to the Lamé coefficients in 2D as:

$$E = \lambda + \mu, \quad G = \mu, \quad K = \frac{4\mu(\lambda+\mu)}{\lambda+2\mu} = \frac{4EG}{E+G}. \tag{S13}$$

Furthermore, from equilibrium statistical thermodynamics the isothermal compressibility $\kappa = 1/E$, where E is the bulk modulus, is expressed as:

$$\frac{1}{E} = \kappa = -\frac{1}{V}\left(\frac{\partial V}{\partial P}\right)_T = \frac{1}{\rho}\left(\frac{\partial \rho}{\partial P}\right)_T, \tag{S14}$$

which can also be measured directly from the slope of $P - \rho$ curves. Once the uniform pressure of the system and the stiffness tensor (or the effective stiffness tensor $\mathbb{B}$) are known, we obtain the elastic moduli from λ and μ using Eq. S13. In our simulations we apply the method of box deformations to numerically evaluate the stiffness tensor for a system of interacting particles in an NVT ensemble [13, 14].

We extract the four non-zero elements of the stiffness tensor $\mathbb{C}$ by performing three kinds of deformations of the simulation box following Ref. [14]. In the first kind of deformation, the box is elongated or compressed along the x-direction by a small factor ϵ_{xx} such that the particle coordinates in the x-direction become $x' = x(1+\epsilon_{xx})$ and the box length also becomes $L'_x = L_x(1+\epsilon_{xx})$. Similarly, the box can be elongated or compressed along the y-direction corresponding to imposing a small linear strain ϵ_{yy}. Both these deformations correspond to a change in the overall density of the system but the magnitude is kept small in order to stay in the linear response regime. The third deformation is of a shearing type in which we change the shape of the box by keeping the volume constant. The angle between the x and y dimension box vectors is changed from $\pi/2$ to $\pi/2 - \tan^{-1}(\epsilon_{xy})$. The particle positions are then transformed as $(x, y) \to (x + y\epsilon_{xy}, y)$.

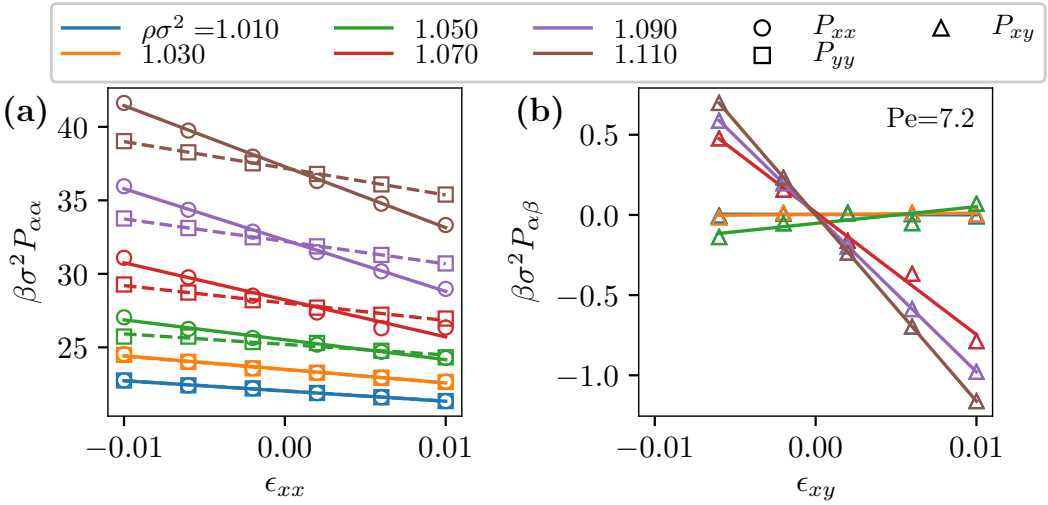

FIG. S7. (a) Diagonal $P_{xx}(\circ), P_{yy}(\square)$ and (b) off-diagonal $P_{xy}(\triangle)$ components of the full pressure tensor (Eq. S8) obtained in a deformed simulation box with $N = 2.8 \times 10^3$ particles as a function of linear tensile and shearing strains, ϵ_{xx} and ϵ_{xy}, respectively, for various state points $\rho\sigma^2$ as labeled in the legend for Pe = 7.2. The stress response is linear in this regime of small strain magnitudes. We obtain the elements of the effective stiffness tensor $\mathbb{B}$ from the slope of a linear fit (solid and dashed lines) to the data points (symbols). The errorbars in the measurements are smaller than the symbol sizes.

In our simulations, we start from a perfect hexagonal initial configuration with $N = 2.8 \times 10^3$ particles and deform the box corresponding to the applied strain. We then measure the full stress tensor $P_{\alpha\beta}$ after a sufficiently long equilibration time that allows the system to reach a steady state. We perform the measurements by applying fixed linear strain $\epsilon_{xx} \in [-0.01, 0.01]$ in intervals of 0.004. For an isotropic solid only the first two elements C_{11} and C_{12} are sufficient to obtain the Lamé coefficients λ and μ, which can be measured just by applying a longitudinal strain ϵ_{xx}. However, for some cases we also measure the values of μ obtained by imposing a shearing strain ϵ_{xy} and confirm that the two independent measurements agree. The effective stiffness tensor $\mathbb{B}$ is directly obtained from the slope of a linear fit to the stress vs. strain curves, as shown for B_{11}, B_{12} and B_{44} in Fig. S7, using

$$B_{11} = \frac{\partial P_{xx}}{\partial \epsilon_{xx}}, \quad B_{22} = \frac{\partial P_{yy}}{\partial \epsilon_{yy}}, \quad B_{12} = \frac{\partial P_{yy}}{\partial \epsilon_{xx}}, \quad B_{44} = \frac{\partial P_{xy}}{\partial \epsilon_{xy}},$$

C. Bulk and Shear elastic moduli

In Fig. S8(a) and S8(b) we plot the bulk modulus E and the shear modulus G, respectively, as a function of density for various Pe obtained using the method described above. For Pe = 0 (magnified in the inset) we find that there is a distinct jump in both E and G, as indicated in the figure by a blue arrow, at a density of $\rho\sigma^2 = 0.926$. This jump is indicative of the second order nature of the transition. Upon increasing Pe, we observe a similar jump appearing in both E and G at higher densities marked by arrows in the figure. The bulk modulus E shows only a discontinuity for higher Pe but the shear modulus G shows a sharp drop to very small values at this transition upon reducing the density. Such a small value of the shear modulus G indicates that the system is not a solid anymore and undergoes plastic deformation upon shearing. Furthermore, in the same plots we also indicate the densities where we observe a finite number of defects in the simulations with $N = 2.8 \times 10^3$ particles by a plus marker (+) as in the main text Fig. 4(a). These points were determined by analyzing the sampled snapshots within our simulated time which show a complete absence of defects at densities higher than the marked points (+).

For Pe = 0 the defects disappear at a density of $\rho\sigma^2 = 0.950$ which is much higher than the point $\rho\sigma^2 = 0.926$ at which we observe the jump in the elastic moduli. For Pe ≥ 7.2 we find that the two transition points agree extremely well. This indicates that for active cases the system becomes plastic as soon as a finite number of defects, mainly dislocations, appear in the system. On the other hand, the elastic moduli of the active solid states as a function of density collapse onto a single master curve independent of Pe. This remarkable result can be explained by the fact that the swim contribution to the stress tensor is zero or negligible in the solid phase, and hence, the elastic constants of active solids become equal to those of passive solids at the same density. The sole effect of activity is that the stable solid regime shifts to higher densities with activity. A numerical fit of the form $E, G \propto \exp(a\rho^3 + b\rho^2 + c\rho + d)$ is shown as a black solid line in both Fig. S8(a) and Fig. S8(b), and agrees very well with the measurements.

V. RENORMALIZATION PROCEDURE FROM KTHNY THEORY

In equilibrium systems, the KTHNY theory suggests that the melting transition is accompanied by a lowering of the Young's modulus βK below a critical value of 16π. To correct for the interactions of defects present at a finite temperature a renormalization group analysis is applied to obtain the renormalized value K_R of the Young's modulus which can then be compared against the numerical value of 16π to identify the melting transition. The theory describes the dislocation defects in 2D systems associated with a 'core energy' E_c [15, 16]. The probability of finding a bound pair of such dislocation defects is given by [17, 18]:

$$\begin{aligned} p_d &= \exp(-2\beta E_c) Z(K) \\ &= \exp\left(-\frac{2E_c}{k_B T}\right) \frac{2\pi\sqrt{3}}{\beta K/8\pi - 1} I_0\left(\frac{\beta K}{8\pi}\right) \exp\left(\frac{\beta K}{8\pi}\right) \end{aligned} \tag{S15}$$

where $Z(K)$ is the internal partition function of a dislocation, and I_0 is a modified Bessel function. The theory suggests a continuous transition from the solid to the hexatic state for large core energies $E_c \geq 2.8 k_B T$ and a weakly to strongly first-order transition as E_c approaches and becomes lower than a value of $2.8 k_B T$ [19]. Typically, for systems with hard-core interactions the value of E_c near the solid-hexatic transition is $\sim 6 k_B T$ as found in Ref. [20] for monolayers of hard spheres.

The renormalization group recursion relations for the Young's modulus K are expressed as [15, 16, 18]:

$$\frac{\partial}{\partial l}\left(\frac{8\pi}{\beta K(l)}\right) = 24\pi^2 y^2 \exp\left(\frac{\beta K}{8\pi}\right)\left[0.5 I_0\left(\frac{\beta K}{8\pi}\right) - 0.25 I_1\left(\frac{\beta K}{8\pi}\right)\right] \tag{S16}$$

$$\frac{\partial y(l)}{\partial l} = \left(2 - \frac{\beta K}{8\pi}\right) y + 2\pi y^2 \exp\left(\frac{\beta K}{16\pi}\right) I_0\left(\frac{\beta K}{8\pi}\right). \tag{S17}$$

where the fugacity y of the dislocation-pair fluid is obtained from an estimate of the core energy E_c as:

$$y = \exp\left(-\frac{E_c}{k_B T}\right). \tag{S18}$$

The differential equations Eq. S16-S17 can be solved recursively for $l = 0 \ldots \infty$ by using the unrenormalized ('bare') values $K(0) = K$ and $y(0) = \exp(-E_c(K(0)))$ as the initial guesses for $l = 0$ and utilizing a trapezoidal (or higher order scheme) for performing the integration. The renormalized values are obtained from the renormalization-flow diagram of y-vs-$1/K$ (Fig. 1 in Ref. [18]) for the separatrix and $K_R = K(\infty)$ when $y(\infty) = 0$. Exactly at the

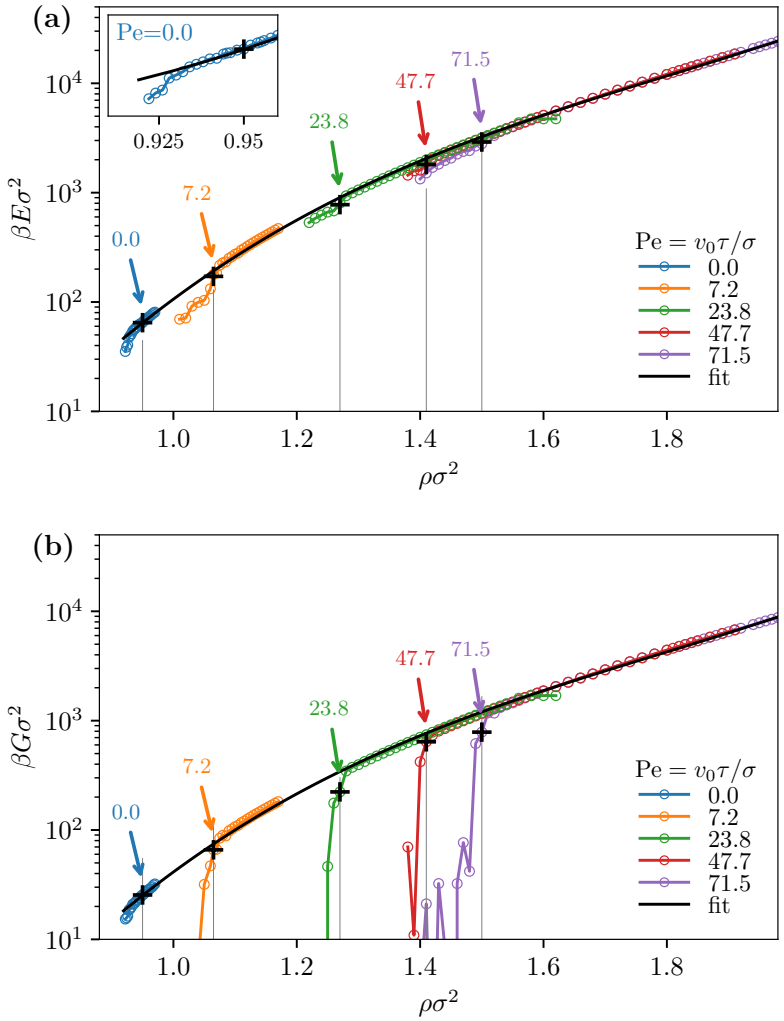

FIG. S8. (a) Bulk modulus E and (b) shear modulus G, obtained by explicitly straining the simulation box with $N = 2.8 \times 10^3$ particles, as a function of density $\rho\sigma^2$ for various Pe as labeled in the legend. Both the bulk and the shear moduli collapse onto a single master curve indicated by the black lines which are fits of the form $E, G \propto \exp(a\rho^3 + b\rho^2 + c\rho + d)$. Upon lowering the density, the shear modulus G drops sharply to zero at the critical density where the defects start to appear for the corresponding activity, and the bulk modulus E shows a transition to a lower stable curve. The transition points at which the defect concentration becomes zero obtained from visual inspection in a system of $N = 2.8 \times 10^3$ particles are marked with a plus (+).

transition, the renormalization-flow follows the separatrix and above ($T > T_m$) and below ($T < T_m$) the melting point goes to the end points ∞ and 0, respectively.

[1] G. S. Redner, M. F. Hagan, and A. Baskaran, Phys. Rev. Lett. **110**, 55701 (2013).
[2] J. A. Anderson, C. D. Lorenz, and A. Travesset, J. Comput. Phys. **227**, 5342 (2008).
[3] J. Glaser, T. D. Nguyen, J. A. Anderson, P. Liu, F. Spiga, J. A. Millan, D. C. Morse, and S. C. Glotzer, Comput. Phys. Commun. **192**, 97 (2015).
[4] P. Digregorio, D. Levis, A. Suma, L. F. Cugliandolo, G. Gonnella, and I. Pagonabarraga, Phys. Rev. Lett. **121**, 098003 (2018).
[5] L. F. Cugliandolo, P. Digregorio, G. Gonnella, and A. Suma, Phys. Rev. Lett. **119**, 268002 (2017).
[6] S. Plimpton, Journal of computational physics **117**, 1 (1995).
[7] R. G. Winkler, A. Wysocki, and G. Gompper, Soft Matter **11**, 6680 (2015).

[8] X. Yang, M. L. Manning, and M. C. Marchetti, Soft Matter **10**, 6477 (2014).
[9] W. Yan and J. F. Brady, New Journal of Physics **20**, 053056 (2018).
[10] A. Sokolov, L. D. Rubio, J. F. Brady, and I. S. Aranson, Nature communications **9**, 1322 (2018).
[11] L. Landau, E. Lifshitz, and J. Sykes, *Theory of Elasticity*, Course of theoretical physics (Pergamon Press, 1989).
[12] J. R. Ray, Comput. Phys. Rep. **8**, 109 (1988).
[13] D. Frenkel and B. Smit, *Understanding molecular simulation: from algorithms to applications*, Vol. 1 (Elsevier, 2001).
[14] G. Clavier, N. Desbiens, E. Bourasseau, V. Lachet, N. Brusselle-Dupend, and B. Rousseau, Mol. Simul. **43**, 1413 (2017).
[15] J. M. Kosterlitz and D. J. Thouless, J. Phys. C Solid State Phys. **6**, 1181 (1973).
[16] D. R. Nelson and B. I. Halperin, Phys. Rev. B **19**, 2457 (1979).
[17] D. S. Fisher, B. I. Halperin, and R. Morf, Phys. Rev. B **20**, 4692 (1979).
[18] S. Sengupta, P. Nielaba, and K. Binder, Phys. Rev. E **61**, 6294 (2000).
[19] K. J. Strandburg, Rev. Mod. Phys. **60**, 161 (1988).
[20] W. Qi, A. P. Gantapara, and M. Dijkstra, Soft Matter **10**, 5449 (2014).